MODELLING THE HYPER-VISCOELASTIC BEHAVIOUR OF POLYURETHANE RUBBERS USING QUASI-STATIC AND DYNAMIC LOADING

Carlos Andrade[1], João Barros[2], Diogo Neto[1], Amílcar Ramalho[1], Marta Oliveira[1]

1: CEMMPRE, Department of Mechanical Engineering
University of Coimbra
Polo II, Rua Luís Reis Santos, Pinhal de Marrocos, 3030-788 Coimbra, Portugal
e-mails: carlos.andrade@uc.pt
diogo.neto@dem.uc.pt
amilcar.ramalho@dem.uc.pt
marta.oliveira@dem.uc.pt
web: http://www.uc.pt/en/iii/research_centers/CEMMPRE

2: CMEMS, Microelectromechanical Systems Research Unit
University of Minho
Campus de Azurém, 4800-058 Guimarães, Portugal
e-mail: joao.barros @student.dem.uc.pt
web: http://www.mems.dei.uminho.pt/

Keywords: Rubber pad forming, hyper-viscoelastic behaviour, Mooney-Rivlin model, Maxwell elements

Abstract *The main objective of this study is to calibrate the material parameters of a hyper-viscoelastic constitutive model for two polyurethanes typically used in rubber pad forming. The hyperelastic behavior is described by the Mooney-Rivlin model, while the viscoelasticity is modelled by a series of Maxwell elements. Two different loading modes are considered simultaneously in the calibration process: (i) uniaxial compression and (ii) shear with superimposed normal compression. In order to cover different time scales of response, the calibrations are carried out, for each material, with two types of loading: (i) quasi-static and (ii) dynamic. The calibration of the material parameters is performed using a modified least squares method, minimizing the difference between numerical and experimental first Piola-Kirchhoff stresses .The results show that, in general, the numerical model can reproduce very well the experimental behavior of both rubbers. However, to achieve a good agreement between numerical and experimental results the set of calibrated material parameters has to be different for the quasi-static and dynamic loading.*

1. INTRODUCTION

Presently and considering the scenario of the European Union, road transport contributes to about 20% of the total emissions of carbon dioxide (main greenhouse gas). Therefore, the demand for new clean power technologies is imperative to significantly reduce the emission of pollutants and the dependence on fossil fuels [1]. Accordingly, increasing attention has been given to fuel cell technology in order to replace the internal combustion engines in transportation applications [1][2]. Among the several types of fuel cells [3], the Polymeric Electrolyte Membrane Fuel Cells (PEMFC) are the most promising to replace the internal combustion engines due to fast startup time and high power-to-weight ratio. These fuel cells convert the chemical energy of the fuel (hydrogen) directly and efficiently into electrical energy. Although this is a promising technology, some limitations are still hindering its use on a larger scale, namely the high manufacturing cost and the hydrogen storage difficulties. The bipolar plates (BPPs) are multifunctional components, which supply the reactant gases over the electrodes via flow channels and connect electrically the cathode and the anode, while providing structural support for the membrane-electrode assembly. They are one of the primary components of the PEMFC, comprising most of the total cost. The earlier BPPs were fabricated from graphite, which is chemically stable but exhibits low mechanical strength. Thus, more suitable and cost-effective materials have been used in the production of BPPs, namely metals and composites. Since the high density is an important drawback of metals, ultra-thin sheets have been used to produce BPPs, requiring more sophisticated forming methods than the conventional, such as the rubber pad forming [4][5].

Ultra-thin stamped BPPs obtained from the rubber pad forming process are viewed as a promising alternative to the traditional graphite BPPs in PEMFC [3]. The rubber pad forming process uses only a single rigid die, while the other die is replaced by a rubber pad (enclosed in a container), which improves the formability of the blank and the surface quality in comparison with the traditional forming process [6]. However, the forming of ultra-thin BPPs is prone to some forming defects, such as springback, wrinkles, thinning and fracture [7]. Among the several process parameters, the geometry of the forming (rigid) tool and the rubber pad are the most important. Indeed, the mechanical behavior of the rubber material (chemical composition and hardness) is crucial to produce the desired BPP shape without defects [8][9]. Nowadays, the design and optimization of forming processes is carried out by numerical simulation, allowing to reduce the product development time and the manufacturing costs. However, the accuracy of the numerical solutions is strongly dependent on the numerical models used in the finite element simulation [10].

The numerical simulation of the rubber pad forming process requires the modelling of the mechanical behavior of thin metallic sheets (elastoplastic behavior) but also of the rubber pad. The mechanical behavior of rubber-like materials is both elastic and viscous. Regarding the elastic response, it is path-independent, since the work done by the stresses during a deformation process is dictated only by the initial and final configurations, showing a non-linear stress-strain relationship, referred as hyperelastic behavior [11]. The stress-strain relationship in rubber-like materials is derived from a strain energy density function, where the Ogden [12], Mooney-Rivlin [13][14] and Yeoh [15] hyperelastic models are the most widely used. The

modelling of the viscoelastic behavior is significantly more complex than the hyperelastic one due to the rate-dependent response [16]. Indeed, the time-dependent stress-strain relationship in viscoelastic materials presents three important properties: stress relaxation (maintaining a constant strain results in decreasing the stress), creep (maintaining a constant stress results in an increasing strain) and hysteresis (a stress-strain phase lag) [17]. The treatment of the viscoelasticity using phenomenological models considers the material as a continuum and focuses on the curve-fitting of the mechanical behavior through experimental data. Usually, the constitutive relations for viscoelasticity combine the elastic component with the time-dependent viscous effect [18]. One of the most common ways to model the viscoelastic effect is the linear viscoelasticity theory, whose foundations were presented by Coleman et al. [19]. The mechanical modelling of the elastic and viscous effects is typically represented by rheological models, which consist of combinations of springs (elasticity) and dashpots (viscous dissipation). For linear viscoelastic response, some of the most well-known are the Maxwell, Kelvin-Voigt and Zener models [20].

Most of the numerical studies on rubber-like materials take into account only the hyperelastic constitutive modelling [21][22][23][24][25]. On the other hand, the calibration of the material parameters is usually performed based on a single loading mode, typically uniaxial compression/tension [26][27]. However, adopting a single loading mode in the material parameters calibration can lead to incorrect predictions of the material behavior for different loading modes, such as shear and equi-biaxial tension/compression [28]. Therefore, the calibration process for these material models should include simultaneously different loading modes, in order to describe accurately the mechanical behavior of the rubber material. The main objective of this study is to calibrate the material parameters of a hyper-viscoelastic constitutive model for two polyurethane rubbers, which are typically used in rubber pad forming. Two loading modes are considered simultaneously in the calibration process: (i) uniaxial compression and (ii) shear with superimposed normal compression. The hyperelastic behavior is described by the Mooney-Rivlin model while the viscoelasticity is modelled by a series of Maxwell elements. Moreover, in order to cover different time scales of response, both quasi-static and dynamic loadings are used in the calibration of each rubber. The calibration of the material parameters is performed using a modified least squares method, minimizing the difference between numerical and experimental stress values.

The present paper is divided in five sections. Section 2 is dedicated to the mathematical description of the hyperelasticity, viscoelasticity and total numerical stress calculation. The strain measures associated to each loading mode are defined and the numerical stresses are derived considering material isotropy and incompressibility. Section 3 describes the materials and specimen geometries used in the mechanical tests and the experimental procedure followed for each loading mode, for both types of loading. It is also presented the objective function, whose minimization allows to determine the material parameters, as well as several important aspects to take into account regarding the calibration process. In Section 4 the experimental and numerical results are presented and discussed. The mechanical response of both rubbers is compared and their strain-rate sensitivity is assessed. The numerical curves obtained from the calibration processes are compared with the corresponding experimental evolutions, allowing to evaluate the capability of the hyper-viscoelastic model to capture both rubber's behavior.

Finally, the concluding remarks of this study are presented in Section 5.

2. HYPER-VISCOELASTIC CONSTITUTIVE MODELLING

The mechanical behavior of the two polyurethane rubbers is described by a rheological analogy known in the literature as generalized Maxwell model (see Figure 1). This model is defined by an elastic spring (hyperelastic behavior) in parallel with *N* Maxwell elements (viscoelasticity), where each Maxwell element is composed by an elastic spring and a viscous Newton-element in series.

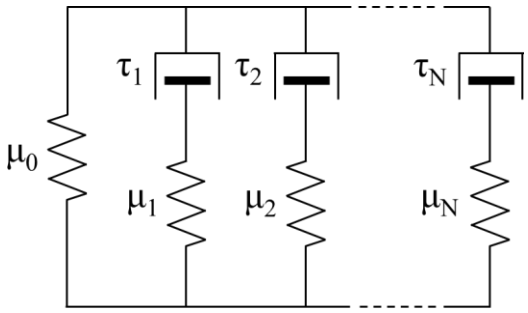

Figure 1. Generalized Maxwell model.

2.1. Hyperelasticity

Materials that recover totally their initial geometry after the deformation is removed are known as elastic. The finite deformation of a material body is usually described using the deformation gradient tensor $\mathbf{F}$, which establishes a correspondence between the position of the material points in the reference configuration ($\mathbf{X}$) and their position in the current configuration ($\mathbf{x}$):

$$\mathbf{F} = \frac{\partial \mathbf{x}}{\partial \mathbf{X}}. \tag{1}$$

This tensor can be decomposed, using the polar decomposition theorem, into a product of two second-order tensors:

$$\mathbf{F} = \mathbf{R}\mathbf{U}, \tag{2}$$

where $\mathbf{R}$ is a proper orthogonal tensor, representing a rotation, and $\mathbf{U}$ is the right stretch tensor. It is also useful to introduce the right Cauchy–Green deformation tensor, given by:

$$\mathbf{C} = \mathbf{F}^{\mathrm{T}}\mathbf{F} = \mathbf{U}^2, \tag{3}$$

where the eigenvalues of $\mathbf{U}$ are the principal stretches λ_i, with i =1,2,3 (the eigenvalues of $\mathbf{C}$ are the squares of the principal stretches). The invariants of $\mathbf{C}$ are defined in the following manner:

$$I_1 = tr(\mathbf{C}) = \lambda_1^{\,2} + \lambda_2^{\,2} + \lambda_3^{\,2}, \tag{4}$$

$$I_2 = \frac{1}{2}(I_1^2 - \mathbf{C}:\mathbf{C}) = \lambda_1^2\lambda_2^2 + \lambda_2^2\lambda_3^2 + \lambda_3^2\lambda_1^2, \tag{5}$$

$$I_3 = \det(\mathbf{C}) = \lambda_1\lambda_2\lambda_3. \tag{6}$$

For hyperelastic materials, different stress measures can be obtained by taking the derivative of the elastic potential with respect to an appropriate deformation measure. The second Piola-Kirchhoff stress tensor $\mathbf{S}$ is determined by differentiating the elastic potential, Ψ, with respect to $\mathbf{C}$:

$$\mathbf{S} = 2\frac{\partial \Psi}{\partial \mathbf{C}}. \tag{7}$$

If the material is assumed isotropic, the elastic potential can be expressed only as a function of the invariants of $\mathbf{C}$ and the reference configuration:

$$\Psi(\mathbf{C}, \mathbf{X}) = \Psi(I_1, I_2, I_3, \mathbf{X}). \tag{8}$$

Considering that the material is incompressible or nearly incompressible, the deformation gradient tensor can be multiplicatively separated into a volumetric component $\mathbf{F}_{\text{vol}}$ and a deviatoric contribution $\bar{\mathbf{F}}$:

$$\mathbf{F} = \mathbf{F}_{\text{vol}}\bar{\mathbf{F}} = (J^{1/3}\mathbf{I})(J^{-1/3}\mathbf{F}), \tag{9}$$

where $J = \det(\mathbf{F})$ and $\mathbf{I}$ is the second-order identity tensor. The same decomposition can be applied to $\mathbf{C}$ in order to obtain the deviatoric right Cauchy-Green deformation tensor $\bar{\mathbf{C}}$:

$$\bar{\mathbf{C}} = J^{-2/3}\mathbf{C}. \tag{10}$$

The invariants of $\bar{\mathbf{C}}$ are related to the invariants of $\mathbf{C}$ by the following equations:

$$\bar{I}_1 = J^{-\frac{2}{3}}I_1, \tag{11}$$

$$\bar{I}_2 = J^{-\frac{4}{3}}I_2, \tag{12}$$

$$\bar{I}_3 = \det(\bar{\mathbf{F}}) = 1. \tag{13}$$

According to [11], the distortional (or isochoric) component of the elastic potential $\bar{\Psi}$ is given by:

$$\bar{\Psi}(\mathbf{C}) = \Psi(\bar{\mathbf{C}}). \tag{14}$$

Therefore, for homogeneous solids with nonlinear elastic behavior, the second Piola-Kirchhoff stress can be expressed by the sum of an isochoric component, $\mathbf{S}_{\text{iso}}$, and a volumetric component, $\mathbf{S}_{\text{vol}}$, such as:

$$\mathbf{S} = \mathbf{S}_{\text{iso}} + \mathbf{S}_{\text{vol}} = 2\frac{\partial \bar{\Psi}}{\partial \bar{\mathbf{C}}} : \frac{\partial \bar{\mathbf{C}}}{\partial \mathbf{C}} + 2\frac{\partial \Psi_{\text{vol}}}{\partial J}\frac{\partial J}{\partial \mathbf{C}}, \tag{15}$$

where Ψ_{vol} is the volumetric component of the elastic potential. Considering the material incompressibility condition (the volume does not change during the deformation) the second Piola-Kirchhoff stress is given by:

$$\mathbf{S} = 2\frac{\partial \bar{\Psi}}{\partial \mathbf{C}} - p\mathbf{C}^{-1}, \tag{16}$$

where p represents the Lagrange multiplier (scalar), which enforces the incompressibility condition. Therefore, the second Piola-Kirchhoff stress tensor for hyperelastic isotropic and incompressible materials is expressed by:

$$\mathbf{S} = 2\left(\frac{\partial \bar{\Psi}}{\partial I_1}\frac{\partial I_1}{\partial \mathbf{C}} + \frac{\partial \bar{\Psi}}{\partial I_2}\frac{\partial I_2}{\partial \mathbf{C}}\right) - p\mathbf{C}^{-1}, \tag{17}$$

with

$$\frac{\partial I_1}{\partial \mathbf{C}} = \mathbf{I}, \tag{18}$$

$$\frac{\partial I_2}{\partial \mathbf{C}} = I_1\mathbf{I} - \mathbf{C}. \tag{19}$$

In this study, the hyperelastic response of the rubbers is described by the Mooney-Rivlin strain energy density function with two parameters, whose deviatoric strain energy density is given by:

$$\bar{\Psi}_{\text{MR}}(\mathbf{C}) = C_{10}(I_1 - 3) + C_{01}(I_2 - 3), \tag{20}$$

where C_{10} and C_{01} are material parameters. Therefore, considering this model, the partial derivatives of the strain energy density with respect to the first and second invariants are simply the parameters C_{10} and C_{01}, respectively. Thus, the second Piola-Kirchhoff stress tensor is given by:

$$\mathbf{S} = 2\left(C_{10}\mathbf{I} + C_{01}(I_1\mathbf{I} - \mathbf{C})\right) - p\mathbf{C}^{-1}. \tag{21}$$

2.2. Viscoelasticity

In order to capture the time-effect dependency of rubber-like materials it is necessary to introduce a viscous effect in the constitutive model. Representing the viscoelastic material response with the linear viscoelasticity theory, a hereditary integral can be used to describe the evolution of the stress with time [29]. Consider the stress $\sigma_i(t)$, at time *t*, due to the application of a strain increment $\Delta\varepsilon_i$, at a time s_i previous to *t*. The stress created by the strain history up to time *t* is given by [30]:

$$\sigma_i(t) = E(t - s_i)\Delta\varepsilon_i\,, \tag{22}$$

where E is the elastic modulus. Following Boltzmann's superposition principle, that states that the effects of sequential variations of deformation are additive, the total stress can be expressed as follows:

$$\sigma(t) = \sum_{i=1}^{M} \sigma_i(t) = \sum_{i=1}^{M} E(t - s_i)\Delta\varepsilon_i\,, \tag{23}$$

As integrals are summing operations, for a linear isotropic viscoelastic body exerting uniaxial stress ($\hat{\sigma}(t)$), the constitutive equation that relates the strain responses can be represented by the hereditary integral [31]:

$$\hat{\sigma}(t) = \int_0^t \hat{\Gamma}(t - s)\frac{\partial\hat{\varepsilon}(s)}{\partial s}\,ds\,, \tag{24}$$

where $\hat{\Gamma}(t - s)$ is a relaxation function given by:

$$\hat{\Gamma}(t - s) = \mu_0 + \sum_{j=1}^{N} \mu_j \exp\left(-\frac{t - s}{\tau_j}\right), \tag{25}$$

where N is the number of Maxwell elements (see Figure 1), μ_0 denotes the time-independent elastic part of the deformation, μ_j is the constant of the j[th] Maxwell elastic spring and τ_j is the dashpot relaxation time of the j[th] Maxwell element. Since $\hat{\sigma}(t)$ is a causal function, the lower terminals in Eq. (24) are set at $t = 0$ [32].

Following the procedure adopted in [31], splitting the integral into an elastic and a viscoelastic contribution, gives:

$$\hat{\sigma}(t) = \hat{\sigma}_0(t) + \sum_{j=1}^{N} \hat{h}_j(t)\,, \tag{26}$$

with

$$\hat{h}_j(t) = \int_0^t ak_j \exp\left(-\frac{t - s}{\tau_j}\right)\frac{\partial\hat{\varepsilon}(s)}{\partial s}\,ds\,, \tag{27}$$

where $ak_i = \mu_i/\mu_0$ denotes the ratio between the constant of the Maxwell elastic spring and the time-independent elastic part of the deformation. Further developments allow to write Eq. (27) incrementally, making it able to be implemented numerically:

$$h_j^{n+1} = \exp\left(-\frac{\Delta t}{\tau_j}\right)h_j^n + \frac{ak_j\tau_j}{\Delta t}\left[1 - \exp\left(-\frac{\Delta t}{\tau_j}\right)\right]\left(\sigma_0{}^{n+1} - \sigma_0{}^n\right), \tag{28}$$

where Δt represents the time increment, σ_0 the elastic stress and the superscript n denotes the current increment. Rearranging equation (28), it is possible to express the stress in the i[th]

Maxwell element at the increment n+1 in terms of the second Piola-Kirchhoff stress in the following form:

$$S_{\mathrm{MW}_i}{}^{n+1} = \exp\left(-\frac{\Delta t}{\tau_i}\right) S_{\mathrm{MW}_i}{}^{n} + \frac{ak_i\tau_i}{\Delta t}\left[1-\exp\left(-\frac{\Delta t}{\tau_i}\right)\right]\left(S_{\mathrm{MR}}{}^{n+1} - S_{\mathrm{MR}}{}^{n}\right), \tag{29}$$

The total second Piola-Kirchhoff stress is given by the sum of the hyperelastic stress and the viscoelastic stress of each Maxwell element:

$$S_{\mathrm{Total}} = S_{\mathrm{MR}} + \sum_{i=1}^{N} S_{\mathrm{MW}_i} \ . \tag{30}$$

2.3. Loading modes

The mechanical tests adopted to calibrate the material parameters of the hyper-viscoelastic constitutive model lead to different stress states. Accordingly, two different loading modes were considered in the calibration: (i) uniaxial compression and (ii) shear with superimposed normal compression.

Assuming the material incompressibility condition, the deformation gradient for the uniaxial compression stress state (along the *yy* direction) takes the following form:

$$\mathbf{F} = \begin{bmatrix} \lambda^{-1/2} & 0 & 0 \\ 0 & \lambda & 0 \\ 0 & 0 & \lambda^{-1/2} \end{bmatrix}, \tag{31}$$

where λ denotes the stretch in the loading direction (ratio between final and initial specimen height). The right Cauchy–Green deformation tensor and its inverse are thus given by:

$$\mathbf{C} = \begin{bmatrix} \lambda^{-1} & 0 & 0 \\ 0 & \lambda^{2} & 0 \\ 0 & 0 & \lambda^{-1} \end{bmatrix}; \ \mathbf{C}^{-1} = \begin{bmatrix} \lambda & 0 & 0 \\ 0 & \lambda^{-2} & 0 \\ 0 & 0 & \lambda \end{bmatrix}. \tag{32}$$

Recalling Eq. (21) and taking into account Eq. (30), the second Piola-Kirchhoff stress tensor for the uniaxial stress state is given by:

$$\mathbf{S} = \begin{bmatrix} 2C_{10} + 2C_{01}(\lambda^2 + \lambda^{-1}) - p\lambda & 0 & 0 \\ 0 & 2C_{10} + 4C_{01}\lambda^{-1} - p\lambda^{-2} & 0 \\ 0 & 0 & 2C_{10} + 2C_{01}(\lambda^2 + \lambda^{-1}) - p\lambda \end{bmatrix}. \tag{33}$$

But, according to the test stress state, only $S_{22} \neq 0$. Thus, p can be determined by imposing $S_{11} = S_{33} = 0$:

$$p = 2C_{10}\lambda^{-1} + 2C_{01}(\lambda + \lambda^{-2}) \, . \tag{34}$$

The hyperelastic second Piola-Kirchhoff stress in the loading direction is thus given by:

$$S_{22} = 2C_{10} + 2C_{01}\lambda^{-1} - 2C_{10}\lambda^{-3} - 2C_{01}\lambda^{-4} = 2(C_{10}\lambda + C_{01})(\lambda^{-1} - \lambda^{-4}) . \quad (35)$$

Considering the shear stress under superimposed normal compression stress, the arising stress state is multiaxial. Assuming that the shear occurs in the *xy* plane and the compression in the *yy* direction, the deformation gradient takes the following form (assuming incompressibility conditions):

$$\mathbf{F} = \begin{bmatrix} \lambda^{-1/2} & \lambda\gamma & 0 \\ 0 & \lambda & 0 \\ 0 & 0 & \lambda^{-1/2} \end{bmatrix}, \quad (36)$$

where λ is the stretch in the direction of compression and γ represents the shear parameter, determined by normalizing the amount of shear (total shear displacement in the direction of the *xx* axis) by the height of the tested specimen. The right Cauchy–Green deformation tensor and its inverse are given by:

$$\mathbf{C} = \begin{bmatrix} \lambda^{-1} & \lambda^{1/2}\gamma & 0 \\ \lambda^{1/2}\gamma & \lambda^{2}(\gamma^{2}+1) & 0 \\ 0 & 0 & \lambda^{-1} \end{bmatrix}; \ \mathbf{C}^{-1} = \begin{bmatrix} \lambda(\gamma^{2}+1) & -\lambda^{-1/2}\gamma & 0 \\ -\lambda^{-1/2}\gamma & \lambda^{-2} & 0 \\ 0 & 0 & \lambda \end{bmatrix}. \quad (37)$$

The hyperelastic second Piola-Kirchhoff stress tensor for this loading mode is given by:

$$\mathbf{S} = \begin{bmatrix} 2(C_{10} + C_{01}(I_1 - \lambda^{-1})) - p\lambda(\gamma^{2}+1) & -2C_{01}\lambda^{1/2}\gamma + p\lambda^{-1/2}\gamma & 0 \\ -2C_{01}\lambda^{1/2}\gamma + p\lambda^{-1/2}\gamma & 2[C_{10} + C_{01}(I_1 - \lambda^{2}(\gamma^{2}+1))] - p\lambda^{-2} & 0 \\ 0 & 0 & 2(C_{10} + C_{01}(I_1 - \lambda^{-1})) - p\lambda \end{bmatrix}. \quad (38)$$

According to the test stress state, the Lagrange multiplier can be determined by imposing $S_{33} = 0$, giving:

$$p = 2\lambda^{-1}(C_{10} + C_{01}I_1) - 2C_{01}\lambda^{-2} . \quad (39)$$

Thus, the hyperelastic in-plane shear component of the second Piola-Kirchhoff stress is given by the following expression:

$$S_{12} = -2C_{01}\lambda^{1/2}\gamma + \left[2\lambda^{-1}(C_{10} + C_{01}I_1) - 2C_{01}\lambda^{-2}\right]\lambda^{-1/2}\gamma , \quad (40)$$

and the hyperelastic compression component of the second Piola-Kirchhoff stress is given by:

$$S_{22} = 2[C_{10} + C_{01}(I_1 - \lambda^{2}(\gamma^{2}+1))] - \left[2\lambda^{-1}(C_{10} + C_{01}I_1) - 2C_{01}\lambda^{-2}\right]\lambda^{-2} , \quad (41)$$

where the first invariant of the right Cauchy-Green deformation tensor for this loading mode is described as follows:

$$I_1 = \lambda^2(\gamma^2 + 1) + 2\lambda^{-1}. \tag{42}$$

3. EXPERIMENTAL TESTS

3.1. Materials and specimen preparation

Two different polyurethane (PUR) rubbers are analyzed in this study. The rubbers present different values of hardness, namely 70 and 95 Shore A. Therefore, hereinafter they will be referred as PUR70 and PUR95. The materials were supplied by Norlene in rod format, presenting 20 mm and 18 mm of nominal diameter for PUR70 and PUR95, respectively.

All the specimens used in this study were obtained from the cylindrical rod. However, different specimen geometries are considered for each mechanical test in order to ensure homogeneous deformation and the desired stress states (see Figure 2). Regarding the uniaxial compression tests, the height (H) of the specimen is approximately 1.5 times its diameter (D) to reduce the barreling effect [33]. In this case, the PUR70 specimen was machined to obtain a diameter similar to the one of the PUR95. For the shear test with superimposed normal compression, the specimen is a cylindrical disk, where the thickness is approximately 25% of the diameter in order to increase the ratio between shear stresses and normal bending stresses as much as possible. The effective dimensions of the tested specimens of the PUR70 and PUR95 for both loading modes are listed in Table 1.

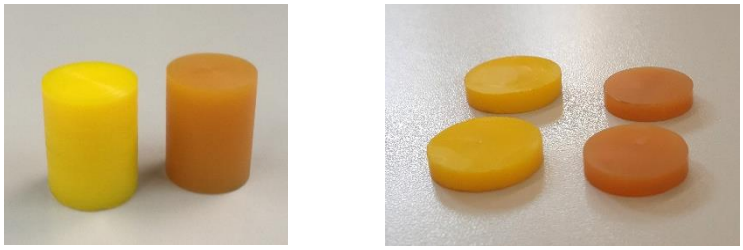

(a) (b)

Figure 2. PUR70 (yellow) and PUR95 (orange) specimens for: (a) Uniaxial compression test; (b) Shear with superimposed normal compression test.

		H [mm]	D [mm]
PUR70	Uniaxial compression	24.4	18.7
	Shear + normal compression	4.8	20.38
PUR95	Uniaxial compression	25.4	18.28
	Shear + normal compression	3.95	18.38

Table 1. Effective dimensions of the tested specimens of the PUR70 and PUR95 for both loading modes and types of loading.

3.2. Experimental procedure

The experimental tests carried out in the present study can be divided into two categories: (i) quasi-static loading and (ii) dynamic loading. All quasi-static tests were conducted on a dual

column electromechanical universal testing machine (Shimadzu) equipped with a 100 kN load cell (±0.5% accuracy). The load and the crosshead displacement were recorded during the tests, allowing to evaluate the evolution of the stress and the deformation. Although this procedure is not the most precise, the instrumentation of strain gauges would be extremely difficult, particularly for the shear with superimposed normal compression test, due to the reduced dimensions of the specimens and the complexity of the assembly (shown in Section 3.2.2). The geometry of the assembly also makes the use of optical strain measurement techniques almost impossible, since there is a limited visibility of the specimens. In the uniaxial compression test, the error committed by using the crosshead displacement is not as significant, since the contact interfaces are lubricated and the strain applied is uniform through the specimen's height. For the quasi-static loading, after the loading phase, a constant deformation period is imposed to evaluate the viscoelastic response of the polyurethanes and their characteristic stress relaxation. In the relaxation period of the shear with superimposed normal compression test, the experimental data points were acquired at a rate of 1 point per second. Regarding the relaxation period of the uniaxial compression test, the acquisition rate was 5 points per second for the PUR95 and 1 point per second for the PUR70.

For the experimental tests with a dynamic load application a free vibration equipment, known as Yerzley oscillograph, was used [34]. The displacement of the equipment's beam and the load acting on the specimen were collected using a displacement sensor and a load cell. The experimental data points of the uniaxial compression and the shear with superimposed normal compression tests were acquired at a rate of 7500 and 10000 points per second, respectively.

3.2.1. Uniaxial compression tests

The experimental apparatus used for the uniaxial compression test under quasi-static loading is shown in Figure 3. In order to reduce the friction between the rubber specimens and the flat compression plates, glycerin was used on the contact interfaces. Hence, the uniaxial stress state is obtained, avoiding the barreling effect. Each uniaxial compression test is composed by two stages: (i) loading phase and (ii) permanency stage. The first stage provides the relationship between the stress and strain, while in the second stage the strain is kept constant during a period of time, allowing for the stress relaxation to occur. Regarding the imposed crosshead speed during the loading stage, it was 5 mm/s and 0.635 mm/s for the PUR70 and PUR95, respectively. This difference of an order of magnitude is due to the very distinct strain rate sensitivity of both materials, which will be explained in detail in section 4.1. The prescribed (maximum) stretch in the uniaxial compression was 0.65 and 0.75 for the PUR70 and PUR95, respectively. Regarding the period of the permanency stage, it is identical for both rubbers, with an imposed value of 200 seconds.

Figure 3. Experimental apparatus used for the uniaxial compression test under quasi-static loading.

The experimental apparatus used for the uniaxial compression test under dynamic loading is based in the Yerzley oscillograph, which is shown in Figure 4. The specimen is placed on one side of the beam, at a known distance to the fulcrum. The masses on the opposite side of the beam create a pre-compression force on the specimen, easily determined by applying the equation of equilibrium of moments. An external perturbation is then applied to the side of the beam that contains the masses, making the system oscillate until all the energy is dissipated (free vibration test). Knowing the displacement of the beam and the dimensions of the lever arms, it was possible to establish the relation to determine the displacement of the specimen.

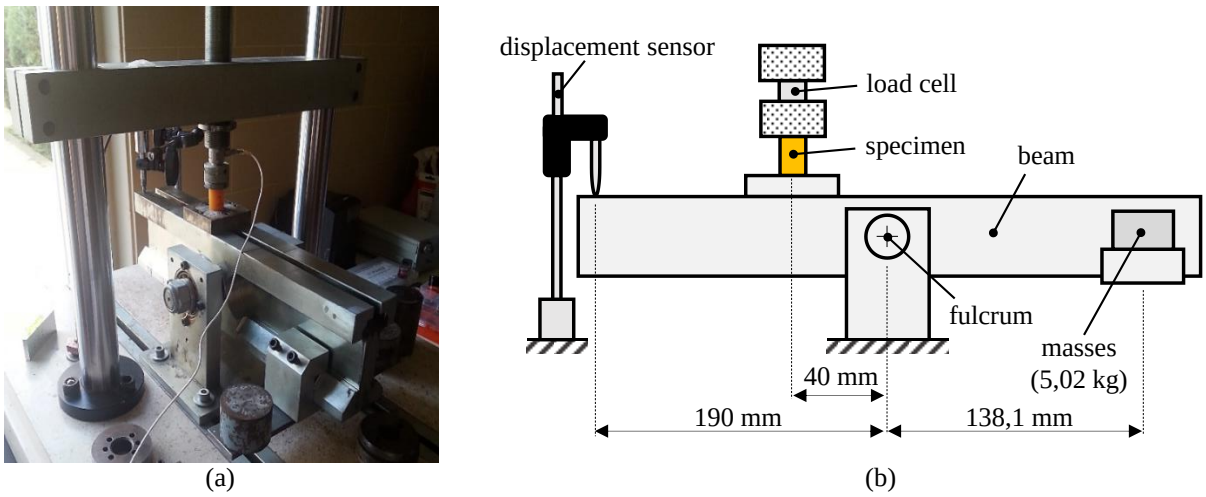

Figure 4. Equipment used for the uniaxial compression test under dynamic loading: (a) Experimental apparatus; (b) Schematic with real dimensions (not at scale).

3.2.2. Shear with superimposed normal compression tests

The experimental apparatus used for the shear with superimposed normal compression tests under quasi-static loading is shown in Figure 5. It was developed specifically to be installed in a universal testing machine. In this test, two identical rubber specimens (see Table 1) are initially compressed between aluminum plates by tightening two bolts. The compression

is carried out by imposing a displacement of 1 mm to each rubber specimen through the exterior plates, i.e. 2 mm reduction of the total height of the assembly. The compression was imposed in approximately 100 s. After approximately 30 s, the central plate was pulled by the testing machine, in a direction perpendicular to the direction of the compression, creating the shear strain on the rubbers. The total prescribed shear displacement (amount of shear) in the loading stage was 0.5 mm, applied in a 10 s time frame. After that, a 200 s stress relaxation period was imposed (equal conditions to both materials).

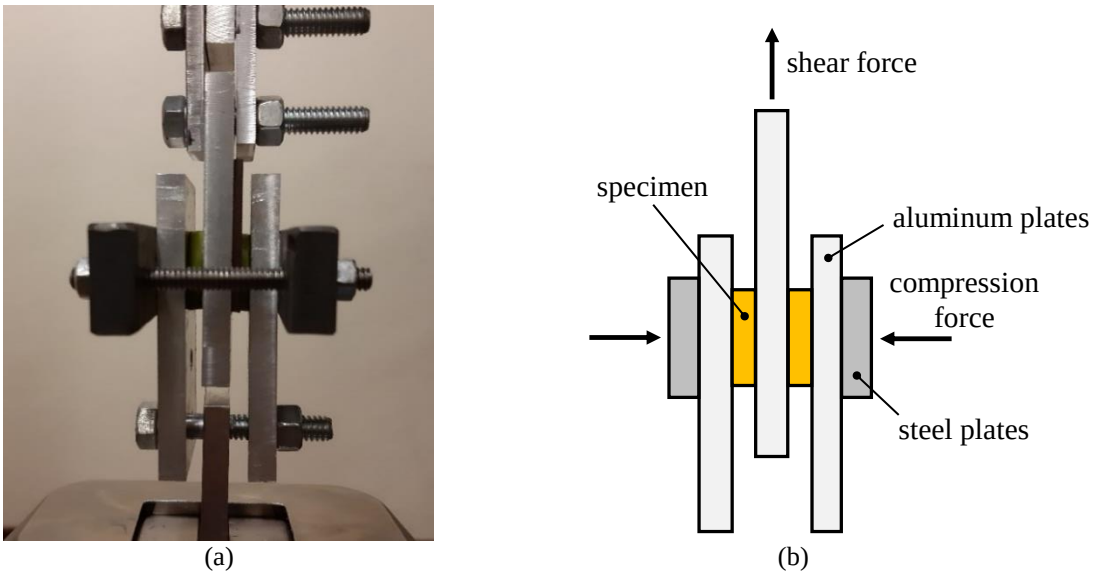

Figure 5. Equipment used for the shear with superimposed normal compression test under quasi-static loading: (a) Experimental apparatus; (b) Schematic.

In order to generate a uniaxial compression stress during the compression phase, the interface between the rubber specimens and the aluminum plates should be frictionless. On the other hand, the creation of the shear stress in the specimen requires a very low slip at the contact interfaces when the central plate is pulled. Therefore, ethyl alcohol was used on the contact interfaces to reduce friction between the rubber specimens and the aluminum plates during the compression phase, while having close to non-lubricated interfaces during the shear loading. Indeed, while an alcohol film is present, a stress state close to uniaxial stress state is obtained in the compression phase, minimizing the barreling effect. After loading, the excess alcohol was removed and the remaining quickly evaporated, allowing friction to exist between the rubber specimens and the plates, which is essential to apply the shear load without the occurrence of slip.

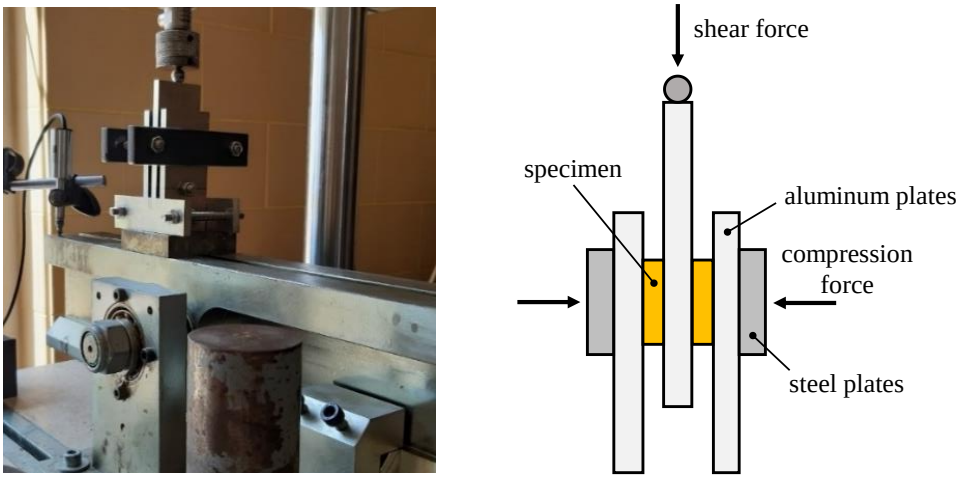

Figure 6. Equipment used for the shear with superimposed normal compression test under dynamic loading: (a) Experimental apparatus; (b) Schematic.

The experimental apparatus used for the shear with superimposed normal compression test under dynamic loading is shown in Figure 6. The experimental conditions are slightly different than the ones used with a quasi-static loading, since the shear load is applied to the specimens by pushing the central aluminum plate instead of pulling it. In order to avoid the generation of unwanted moments, an indentation was made in the top face of the central plate to allow for a steel sphere to be placed there without falling, guaranteeing a point contact for the application of the load. Similarly to the quasi-static loading, during the assembly of the equipment, the compression of the rubber specimens was imposed in 100 s and there was an interval of approximately 30 s before the application of the dynamic loading. The remaining test conditions are the same as indicated for the free vibration test under uniaxial compression (see Figure 4 (b)).

3.3. Calibration of material parameters

The numerical model adopted requires the knowledge of the evolution of the strain measures to calculate the hyperelastic component of the stress (according to Eq. (35) and Eq. (40)). Moreover, it also requires the time step evolution (Eq. (29)), dictated by the acquisition rate of the experimental tests, as the viscoelastic stress of each Maxwell element is calculated since the beginning of the test. The total numerical stress is then calculated and converted from the second to the first Piola-Kirchhoff ($\mathbf{P}$), since only the latter has a physical meaning and can be measured experimentally (force in the current configuration divided by the area in the reference configuration). This conversion is given by:

$$\mathbf{P} = \mathbf{F}\mathbf{S} . \tag{43}$$

Regarding the experimental data used in the calibration of the material parameters, the stress-strain curves are obtained from the force and displacement evolutions, collected during the mechanical tests. The evolution of $\mathbf{P}$ is experimentally evaluated through the

force and initial dimensions of the specimen. The evolutions of the strain measures (stretch and shear parameter) are evaluated through the crosshead speed and time. In the tests performed with a dynamic loading there is always noise present, particularly associated to the sensor of displacement. Despite the application of an arithmetic moving average to the experimental data there is always some noise in these curves, which is propagated to the evolutions of the strain measures and, ultimately, to the evolution of the numerical stress.

The nonlinear least squares fitting was adopted to calibrate the material parameters, comparing the experimental and the numerical first Piola-Kirchhoff stress evolutions:

$$LSM = \min \sum_{i=1}^{n} \left(\alpha_i \sum_{j=1}^{k_i} \left(\frac{P_{\text{exp}}^{(j)} - P_{\text{num}}^{(j)}}{P_{\text{exp,max}}^{(i)}} \right)^2 \right)_i , \tag{44}$$

where n is the number of experimental tests and k_i is the number of data points considered on each test. The subscripts "exp" and "num" denote the experimental and numerical data, respectively, and $P_{\text{exp,max}}^{(i)}$ represents the maximum absolute value of the experimental first Piola-Kirchhoff stress of the i^{th} test. The number of points considered must be a compromise between the accurate description of the mechanical behavior and the time required to perform the minimization. Since the time scale arising in the quasi-static and in the dynamic tests is completely different, the calibration of the material parameters using both loading types simultaneously is not advisable, due to the reduced precision achieved in the description of the mechanical behavior. Therefore, two calibration processes were carried out for each polyurethane, i.e. considering the quasi-static and the dynamic loading. Moreover, in order to give equal contribution to the uniaxial compression and the shear with superimposed normal compression, a weight based on the number of points of each test was applied to each of the calibrations performed ($\alpha_i = k_i / \sum k_i$). The minimization of the distance between each numerical and experimental point requires that they are synchronized in terms of both strain measures and time. In the testing of rubbers under dynamic loading there is always a phase lag between the evolutions of force and displacement (the force and displacement are in phase for an ideal elastic material and are 90º out of phase for an ideal viscous material, assuming intermediate values for a hyper-viscoelastic material). This behavior is inherently present in the calibrations under dynamic loading.

In this paper, the time-effect dependency of both rubbers is assessed through experimental testing of both loading modes at different strain rates. However, in the calibrations only one strain-rate is used for each loading mode. Although the simultaneous calibration of several curves corresponding to different strain-rates could be a possibility, it was not the option considered in this study. Four Maxwell elements were selected to be in parallel with the hyperelastic component, since a lower number was not enough to capture the material behavior accurately and a greater number would not lead to significant improvements. Thus, the calibration procedure for the generalized Maxwell model presented in Section 2 involves the determination of a total of 10 parameters, two relative to the hyperelastic component and two for each Maxwell element. In a general note, it is important to highlight that if the value of the parameter *ak* of a given Maxwell element is small, the effect of the relaxation time τ of that

particular element in the numerical solution is negligible, which means that even if it changes several orders of magnitude it would not have impact in the objective function.

The objective function presented in Eq. (44) was minimized using the Generalized Reduced Gradient (GRG) algorithm. This algorithm does not guarantee the determination of the global minimum of the function, since it can convergence to different local minimum, and is known to be sensitive to the initial solution adopted. Constraints were assigned to the lower limit of all parameters: for the hyperelastic parameters it was imposed $\{C_{10}, C_{01}\} \geq 0$ while for the ones associated with the viscoelasticity it was imposed $ak_i \geq 10^{-5}$ and $\tau_i \geq 10^{-10}$. Several sets of initial parameters were tested under these conditions and the solution always converged to nearly the same set of final parameters in each calibration (residual differences).

4. RESULTS AND DISCUSSION

Due to the very distinct time scales arising in the quasi-static and dynamic loadings, the mechanical behaviour is modelled independently for each loading type in order to achieve better precision of the numerical solution. Accordingly, the calibration of the material parameters is carried out using: (i) the experimental data from the quasi-static mechanical tests and (ii) the experimental data from the dynamic mechanical tests.

4.1. Quasi-static loading

Although both tests are performed under quasi-static conditions, the effect of the strain rate on the mechanical behaviour is assessed by comparing the different test conditions. The rate of the strain measures associated to each test (stretch and shear parameter) is constant throughout the duration of the loading phase, since the displacements are applied linearly.

The experimental stress-stretch curves obtained from the uniaxial compression test for different values of stretch rate are presented in Figure 7 (a) and (b) for the PUR70 and PUR95, respectively. The stretch rates studied range from -0.0011 s^{-1} to -0.2 s^{-1}, which correspond to a crosshead speed of 0.0268 mm/s and 5 mm/s, respectively. Comparing the two rubbers, the effect of the material hardness on the stress is highlighted. Indeed, for the same level of stretch, the stress value in the PUR95 is approximately 3 times higher than the one measured for the PUR70. The influence of the stretch rate on the mechanical response is more pronounced in the PUR95 than in the PUR70, as shown in Figure 7 (for this reason the PUR95 was tested under more values of stretch rate). However, the difference in the stress value is lower than 10% when changing the stretch rate two orders of magnitude. Since the PUR70 rubber is not very stretch-rate sensitive, the highest value (-0.2 s^{-1}) was used in the calibration of the material parameters. For the PUR95 only the lowest and highest stretch rate values (-0.0011 s^{-1} and -0.2 s^{-1}, respectively) show significant discrepancies in comparison with the other three mid-range values studied and, therefore, the intermediate value of -0.025 s^{-1} was adopted in the calibration process.

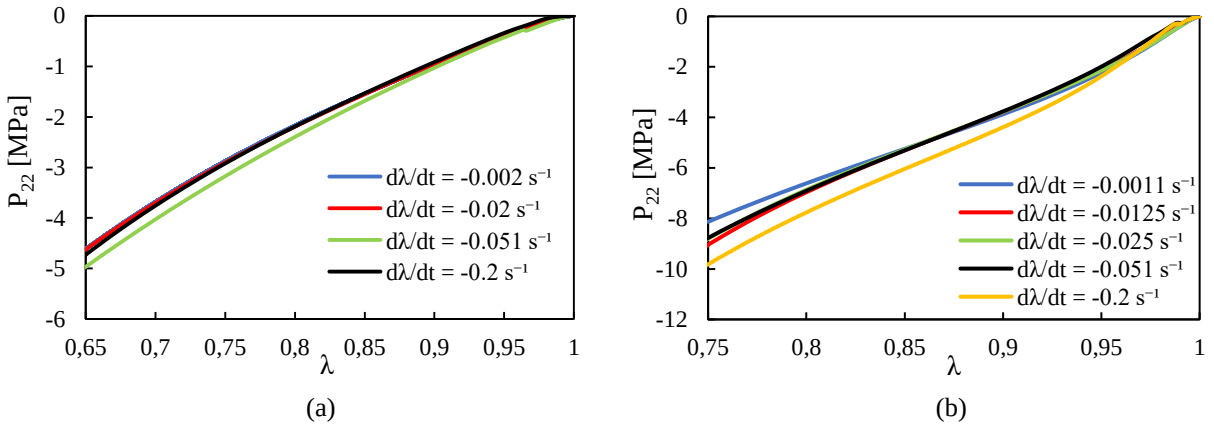

Figure 7. Stretch rate sensitivity in the uniaxial compression test under quasi-static loading: (a) PUR70; (b) PUR95.

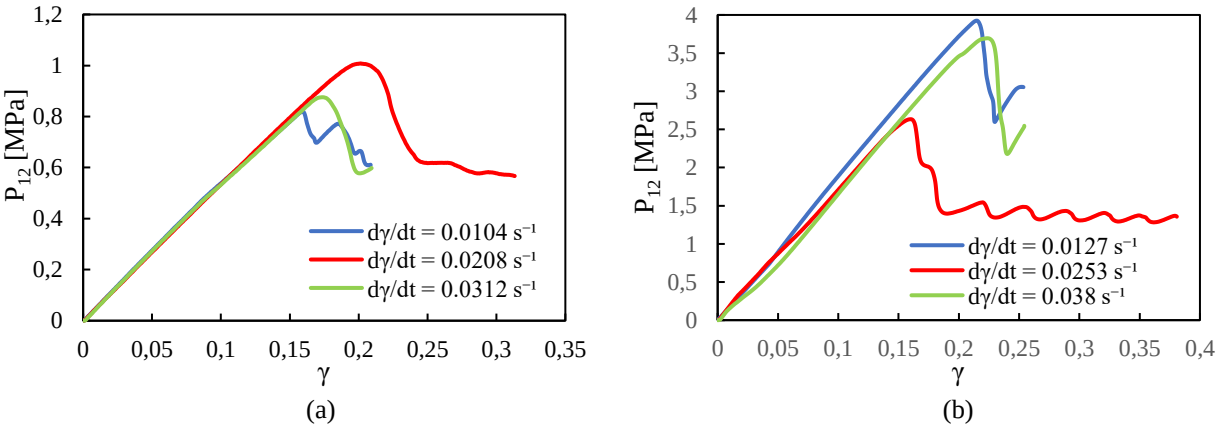

Figure 8. Shear parameter rate sensitivity in the shear with superimposed normal compression test under quasi-static loading: (a) PUR70; (b) PUR95.

Taking into account the geometry of the specimens, the shear parameter's value is derived from the central plate displacement. Note that the meaning of the shear parameter is valid only up to the occurrence of slipping between the specimens and the plates, detected by the drops in the evolution of the stress. The experimental evolution of the shear stress for different values of shear parameter rate, obtained from the shear test with superimposed normal compression, is presented in Figure 8 (a) and (b) for the PUR70 and PUR95, respectively. The shear parameter rates studied range from 0.0104 s^{-1} to 0.038 s^{-1}, which correspond to a crosshead speed of 0.05 mm/s and 0.15 mm/s, respectively. The relationship between the shear stress and the shear parameter is approximately linear up to the beginning of slipping. However, for the same value of shear parameter, the shear stress value in the PUR95 is approximately 3 times higher than the one measured for the PUR70, which is related with the material hardness. The effect of the shear parameter rate value on the shear stress evolution is negligible up to the start of slipping, particularly in the PUR70 (see

Figure 8 (a)). In order to guarantee a valid description of the mechanical response (before slipping), the shear parameter was limited to $\gamma = 0.127$ in a new experimental test used in the calibration procedure, which corresponds to 0.5 mm of imposed displacement in the central plate. The onset of slipping does not show a clear trend in function of the shear parameter rate, which may be a result of different misalignments in the setup (see Figure 8). The lowest value of shear parameter rate was selected for this test considered in the calibration procedure in order to minimize the influence of possible misalignments in the assembly on the mechanical behaviour of the material. This ensures that the following relaxation period is carried our properly, i.e. without slipping between the specimens and the plates.

Considering the uniaxial compression test, the comparison between the experimental and the calibrated normal stress evolution is presented in Figure 9 (a) and Figure 10 (a) for the PUR70 and PUR95, respectively. Regarding the shear test with superimposed normal compression, the comparison between the experimental and the calibrated shear stress evolution is shown in Figure 9 (b) and Figure 10 (b) for the PUR70 and PUR95, respectively. The set of material parameters calibrated for quasi-static loading conditions is listed in Table 2 for both materials (PUR70 and PUR95). Note that, for the PUR95, the parameter C_{01} is zero. In this particular condition, the Mooney-Rivlin equation (Eq. (20)) reduces to the Neo-Hookean formula. Note also that, for both rubbers, the relaxation times (τ_j) assume values of different orders of magnitude, highlighting the importance of considering several Maxwell elements in the calibration in order to achieve significant flexibility in the description of the stress relaxation, capturing both the short and the long-term behavior.

	C_{10}	C_{01}	ak_1	ak_2	ak_3	ak_4	τ_1	τ_2	τ_3	τ_4
PUR70	0.3504	0.49316	0.05584	0.00001	0.10592	0.04575	240.05	0.05173	5042.61	15.62
PUR95	3.7374	0	0.06988	0.11896	0.00001	0.00001	58.2	2.214	2051.3	2.014

Table 2. Calibrated material parameters for the PUR70 and PUR95 under quasi-static loading.

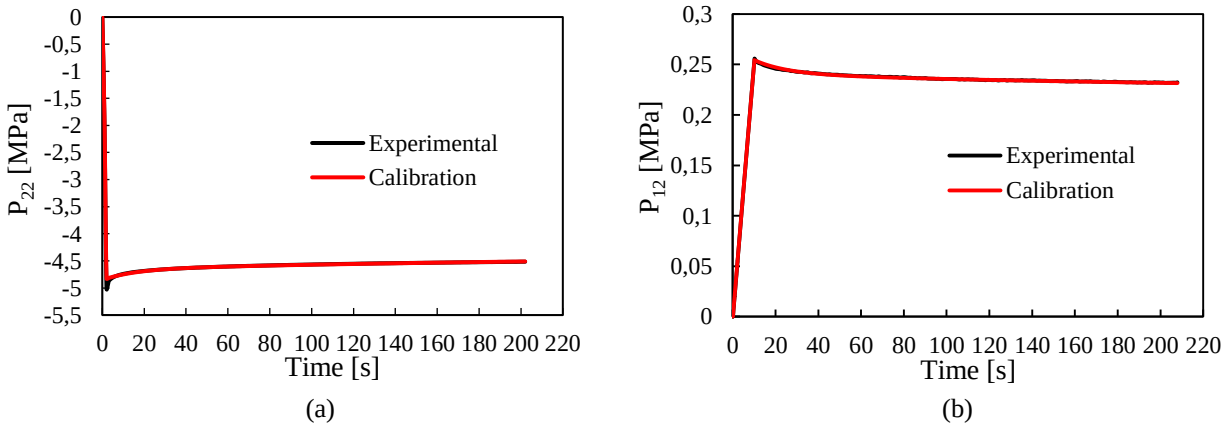

Figure 9. Calibrated curves *versus* experimental curves for the PUR70 under quasi-static loading: (a) Uniaxial compression; (b) Shear with superimposed normal compression.

The mechanical behavior of the PUR70 under quasi-static conditions is accurately predicted by the numerical model described in Section 2, as shown in Figure 9. The difference between the experimental and the numerical response is lower in the shear test with superimposed normal compression. Indeed, the maximum value of stress arising in the uniaxial compression test (end of the loading phase) is underestimated 3.8% (see Figure 9 (a)). This is a result of the low number of points collected in this stage, since the acquisition rate was the same for both loading and relaxation periods and the loading was performed in a short time frame. After the relaxation period of 200 s, the stress in the uniaxial compression test reduced to approximately 90% of the maximum absolute experimental value, while for the shear with superimposed normal compression it reduced to 91%.

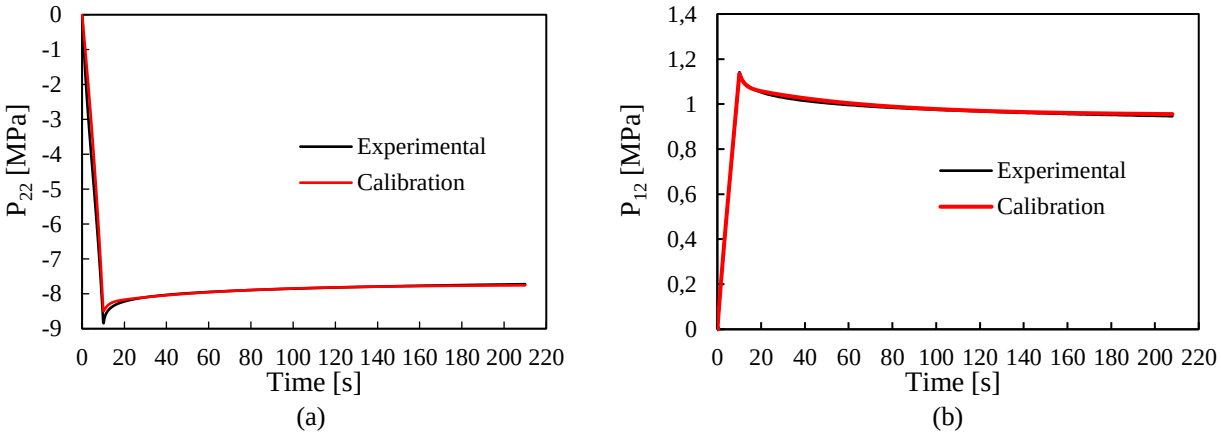

Figure 10. Calibrated curves *versus* experimental curves for the PUR95 under quasi-static loading: (a) Uniaxial compression; (b) Shear with superimposed normal compression.

The same global comments are valid regarding the description of the mechanical behavior of the PUR95 under quasi-static conditions, as shown in Figure 10. After the relaxation period of 200 s, the normal stress (uniaxial compression) reduced to approximately 88% of the maximum absolute value, while the shear stress reduced to 83%. Considering the uniaxial compression test, the experimental stress is underestimated by the model in the loading phase. However, the difference is lower than 3.9% (relative error), which occurs at the end of the loading stage. Nevertheless, the relaxation period is captured with great accuracy. On the other hand, both the loading and the permanency stages are accurately predicted in the shear test with superimposed normal compression (see Figure 10 (b)).

4.2. Dynamic loading

Both the uniaxial compression test and the shear test with superimposed normal compression were carried out also under dynamic loading, using the Yerzley oscillograph. In order to evaluate the reproducibility of the experimental force measurements, three tests were performed under the same conditions for each PUR. Since the initial external perturbation (force) can be different in each test, the oscillatory component of the stress evolution was normalized by its maximum absolute value. Therefore, the stress induced by

the masses was removed from the total measured stress, obtaining the usual response of a free vibration system. This allows for a comparative analysis of the dissipative behavior of each PUR. The normalized first Piola-Kirchhoff stress evolution measured in the PUR70 is presented in Figures 11 (a) and (b) for the uniaxial compression test and the shear test with superimposed normal compression, respectively. The corresponding evolution for the PUR95 is presented in Figures 12 (a) and (b), respectively. The experimental stress and displacement were collected during 2 s, allowing to capture a significant number of periods. However, the comparison of the curves considers only the significant time of each test, which was established as the time required for the normalized stress to get below 5% of the maximum amplitude. These values of time are higher for PUR70 than for PUR95 and, for each material, are higher for the compression test. For both loading modes adopted and for both rubbers, the difference between the three tests is negligible, highlighting the reproducibility of the experimental normalized stress measured.

The calibrated set of material parameters for both PUR70 and PUR95 under dynamic loading is listed in Table 3. Regarding the uniaxial compression test, the comparison between the experimental and the calibrated normal stress evolution is presented in Figure 13 (a) and Figure 14 (a) for the PUR70 and PUR95, respectively, while for the shear test with superimposed normal compression, the comparison between the experimental and the calibrated shear stress evolution is shown in Figure 13 (b) and Figure 14 (b) for the PUR70 and PUR95, respectively.

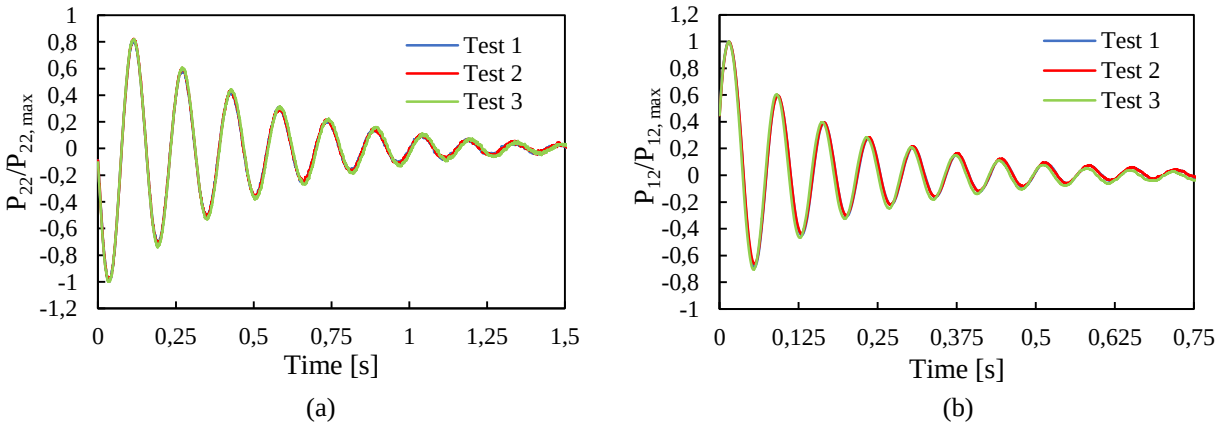

Figure 11. Normalized stress evolution under free vibration of the PUR70: (a) Uniaxial compression; (b) Shear with superimposed normal compression.

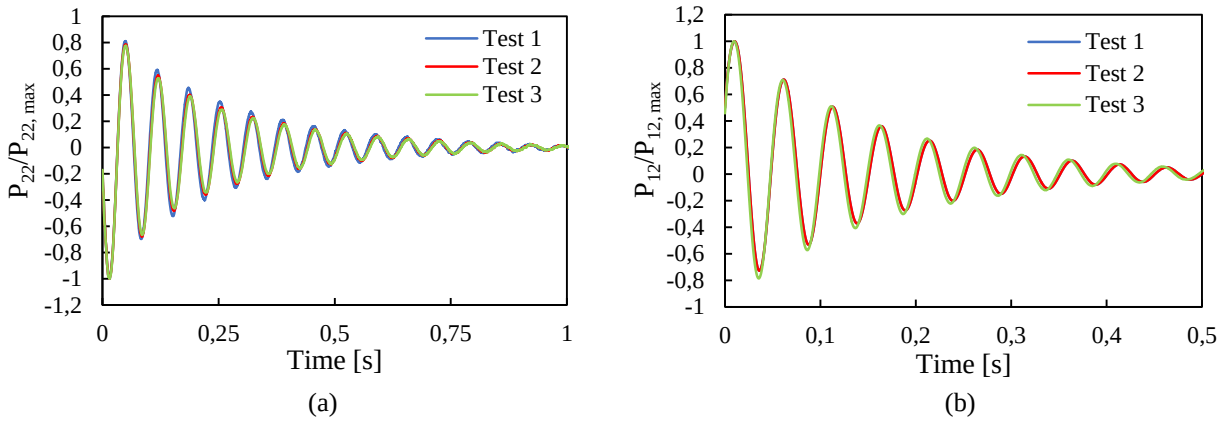

Figure 12. Normalized stress evolution under free vibration of the PUR95: (a) Uniaxial compression; (b) Shear with superimposed normal compression.

	C_{10}	C_{01}	ak_1	ak_2	ak_3	ak_4	τ_1	τ_2	τ_3	τ_4
PUR70	1.3759	0	0.12134	0.00001	1.42071	0.10877	0.00143	2.5793	0.00142	23744.1
PUR95	6.0767	0	0.03528	0.00001	555.22	0.10911	0.00315	4.9948	3.095E-6	166509.1

Table 3. Calibrated material parameters for the PUR70 and PUR95 under dynamic loading.

Note that the parameter C_{01} is zero for both materials, i.e. the Mooney-Rivlin equation (Eq. (20)) reduces to the Neo-Hookean formula. The difference in the rubber's hardness value has a noticeable impact when comparing the values of C_{10}, which are much greater for the PUR95. Also, the relaxation times listed in Table 3 assume, similarly to the quasi-static calibrations, values of very different orders of magnitude. Figure 13 shows clearly that the calibrated material parameters can approximate almost perfectly the behavior of the PUR70 for the two experimental tests performed. For the PUR95, the calibrated material parameters can approximate very precisely the dynamic behavior of the shear with superimposed normal compression test. However, for the uniaxial compression test the calibrated stress curve underestimates the amplitude of the experimental stress.

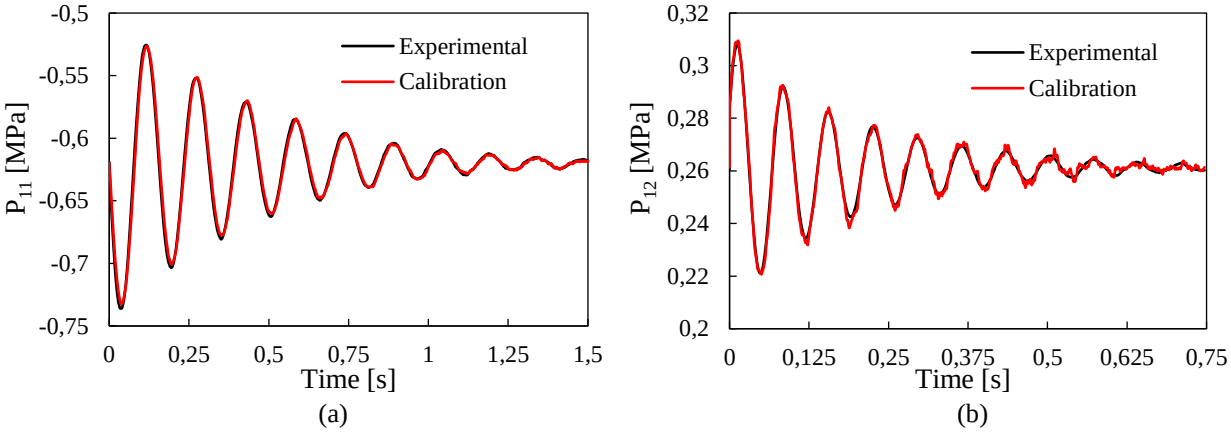

Figure 13. Calibrated curves *versus* experimental curves for the PUR70 under dynamic loading: (a) Uniaxial compression; (b) Shear with superimposed normal compression.

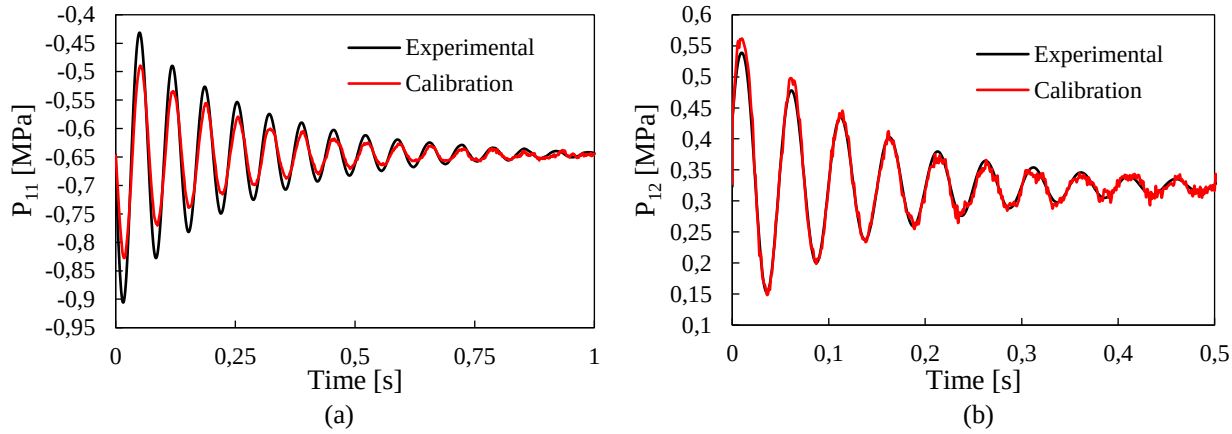

Figure 14. Calibrated curves *versus* experimental curves for the PUR95 under dynamic loading: (a) Uniaxial compression; (b) Shear with superimposed normal compression.

Comparing directly Figure 13 and Figure 14 in terms of each loading mode, it is clear that, for a given instant, the dynamic response of the PUR95 presents a greater number of completed periods, due to its increased stiffness. This is particularly evident in the uniaxial compression test. For each rubber, when comparing both loading modes at a similar instant, a greater number of completed periods is observed in the shear with superimposed normal compression test. Regarding the comparison between the calibrated material parameters for the quasi-static loading (see Table 2) and dynamic loading (see Table 3) one can notice that, for the latter, the parameters associated with the viscoelasticity have a much broader range, with several orders of magnitude of difference between Maxwell elements. As the time scale of the dynamic loading is significantly lower than that of the quasi-static loading, for industrial applications with very high cadence, the calibration of parameters in a dynamic manner can be of particular interest.

5. CONCLUSIONS

This study presents a hyper-viscoelastic constitutive model to characterize the mechanical behavior of two polyurethane rubbers. The hyperelastic component is described by the Mooney-Rivlin model and the viscoelastic component by four Maxwell elements, leading to a total of 10 material parameters. The calibration process is performed by applying the least squares method to fit the first Piola-Kirchhoff stress curves of the model to the experimental curves. Two loading modes were considered, uniaxial compression and shear with superimposed normal compression. Besides, each experimental test is performed under both quasi-static and dynamic loading. For the quasi-static loading, a relaxation period was imposed after the loading phase, allowing for stress relaxation of the polyurethanes. The dynamic loading consisted of free vibration tests to capture the dissipative behavior, performed using Yerzley oscillograph. Since there is a substantial difference in the time frame of the quasi-static and dynamic loading it is not advisable to calibrate these types of loading simultaneously, due to the reduced precision achieved with the numerical solution. Therefore, the calibration of the material parameters was carried out independently for each type of loading. It is very important to know the specific time frame of a certain practical application involving these materials to select the proper set of calibrated parameters.

Experimental tests for both materials with both loading modes at different strain rates allowed to identify the PUR95 as the most strain-rate sensitive rubber. Regarding the calibration processes, the results showed that the calibrated material parameters can reproduce very accurately the mechanical behavior of the PUR70, for both ways of loading. For the PUR95, a good agreement with the experimental results was found for the quasi-static loading. For the dynamic loading calibration, the shear with superimposed normal compression was described accurately, while the uniaxial stress curve underestimates the experimental stress. The calibrated material parameters for the dynamic loading, particularly the ones associated with the viscoelasticity, vary between a broad range of values, with several orders of magnitude of difference between Maxwell elements. For industrial applications with very high cadence of production (few seconds), a dynamic calibration of the parameters can be more suitable to describe the material's behavior.

ACKNOWLEDGEMENTS

The authors would like to acknowledge the funding from of the Foundation for Science and Technology (FCT) under projects PTDC/EMS-TEC/6400/2014 (POCI-01-0145-FEDER-016876), PTDC/EMS-TEC/0702/2014 (POCI-01-0145-FEDER-016779) and PTDC/EMEAPL/29713/2017 (CENTRO-01-0145-FEDER-029713) by UE/FEDER through the program COMPETE 2020. The support under the project MATIS (CENTRO-01-0145-FEDER-000014) and UID/EMS/00285/2020 is also acknowledged.

REFERENCES

1. Wang Y, Chen KS, Mishler J, et al (2011) A review of polymer electrolyte membrane fuel cells: Technology, applications, and needs on fundamental research. Appl Energy 88:981–1007. https://doi.org/10.1016/j.apenergy.2010.09.030

2. Alaswad A, Baroutaji A, Achour H, et al (2016) Developments in fuel cell technologies in the transport sector. Int J Hydrogen Energy 41:16499–16508. https://doi.org/10.1016/j.ijhydene.2016.03.164
3. Giorgi L, Leccese F (2013) Fuel Cells: Technologies and Applications. Open Fuel Cells J 6:1–20. https://doi.org/10.2174/1875932720130719001
4. Lim SS, Kim YT, Kang CG (2013) Fabrication of aluminum 1050 micro-channel proton exchange membrane fuel cell bipolar plate using rubber-pad-forming process. Int J Adv Manuf Technol 65:231–238. https://doi.org/10.1007/s00170-012-4162-8
5. Elyasi M, Khatir FA, Hosseinzadeh M (2017) Manufacturing metallic bipolar plate fuel cells through rubber pad forming process. Int J Adv Manuf Technol 89:3257–3269. https://doi.org/10.1007/s00170-016-9297-6
6. Alo OA, Otunniyi IO, Pienaar HcZ (2019) Manufacturing methods for metallic bipolar plates for polymer electrolyte membrane fuel cell. Mater Manuf Process 34:927–955. https://doi.org/10.1080/10426914.2019.1605170
7. Park W, Jin C, Kang C (2016) Improving channel depth of stainless steel bipolar plate in fuel cell using process parameters of stamping. Int J Adv Manuf Technol 87:. https://doi.org/10.1007/s00170-016-8606-4
8. Tandogan M, Eyercioglu O (2017) Hardness Effect of Polyurethane Rubber on Mesoscale Rubber Pad Forming. Int Adv Res J Sci Eng Technol 4:95–105. https://doi.org/10.17148/IARJSET.2017.4914
9. Jin CK, Jeong MG, Kang CG (2014) Effect of rubber forming process parameters on micro-patterning of thin metallic plates. Procedia Eng 81:1439–1444. https://doi.org/10.1016/j.proeng.2014.10.170
10. Charon W, Iltchev M-C, Blachot J-F (2014) Mechanical simulation of a Proton Exchange Membrane Fuel Cell stack using representative elementary volumes of stamped metallic bipolar plates. Int J Hydrogen Energy 39:13195–13205. https://doi.org/10.1016/j.ijhydene.2014.06.125
11. Bonet J, Wood RD (2008) Nonlinear Continuum Mechanics for Finite Element Analysis, Second Edi. Cambridge University Press
12. Ogden RW (1972) Large Deformation Isotropic Elasticity - on the Correlation of Theory and Experiment for Incompressible Rubberlike Solids. Proc R Soc Lond A Math Phys Sci 326:565–584. https://doi.org/10.5254/1.3542910
13. Mooney M (1940) A Theory of Large Elastic Deformation. J Appl Phys 11:582–592. https://doi.org/10.1063/1.1712836
14. Rivlin RS (1948) Large elastic deformations of isotropic materials IV. further developments of the general theory. Philos Trans R Soc London Ser A, Math Phys Sci 241:
15. Yeoh OH (1993) Some Forms of the Strain Energy Function for Rubber. Rubber Chem Technol 66:754
16. Kaliske M, Nasdala L, Rothert H (2001) On damage modelling for elastic and viscoelastic materials at large strain. Comput Struct 79:2133–2141. https://doi.org/https://doi.org/10.1016/S0045-7949(01)00061-X
17. Banks HT, Hu S, Kenz ZR (2011) A brief review of elasticity and viscoelasticity for

solids. Adv Appl Math Mech 3:1–51. https://doi.org/10.4208/aamm.10-m1030
18. Wu Y, Wang H, Li A (2016) Parameter identification methods for hyperelastic and hyper-viscoelastic models. Appl Sci 6:. https://doi.org/10.3390/app6120386
19. Coleman BD, Noll W (1961) Foundations of Linear Viscoelasticity. Rev Mod Phys 33:239–249. https://doi.org/10.1103/RevModPhys.33.239
20. Hristov J (2019) Linear viscoelastic responses and constitutive equations in terms of fractional operators with non-singular kernels: Pragmatic approach, memory kernel correspondence requirement and analyses. Eur Phys J Plus 134:. https://doi.org/10.1140/epjp/i2019-12697-7
21. Ali A, Hosseini M, Sahari BB (2010) A Review of Constitutive Models for Rubber-Like Materials. Am J Eng Appl Sci 3:232–239. https://doi.org/10.3844/ajeassp.2010.232.239
22. Ogden RW, Saccomandi G, Sgura I (2004) Fitting hyperelastic models to experimental data. Comput Mech 34:484–502. https://doi.org/10.1007/s00466-004-0593-y
23. Sang JB, Sun LF, Xing SF, et al (2014) Mechanical properties of polymer rubber materials based on a new constitutive model. Polym Polym Compos 22:693–698. https://doi.org/10.1177/096739111402200807
24. Nowak Z (2008) Constitutive modelling and parameter identification for rubber-like materials. Eng Trans 56:117–157
25. Szurgott P, Jarzębski Ł (2019) Selection of a hyper-elastic material model – A case study for a polyurethane component. Lat Am J Solids Struct 16:1–16. https://doi.org/10.1590/1679-78255477
26. Carlescu V, Prisacaru G, Olaru ND (2014) FEM simulation on uniaxial tension of hyperelastic elastomers. Appl Mech Mater 659:57–62. https://doi.org/10.4028/www.scientific.net/AMM.659.57
27. Huri D, Mankovits T (2018) Comparison of the material models in rubber finite element analysis. IOP Conf Ser Mater Sci Eng 393:. https://doi.org/10.1088/1757-899X/393/1/012018
28. Keerthiwansa R, Javorik J, Kledrowetz J, Nekoksa P (2018) Elastomer testing: The risk of using only uniaxial data for fitting the Mooney-Rivlin hyperelastic-material model. Mater Technol 52:3–8. https://doi.org/10.17222/mit.2017.085
29. Hristov J (2019) Response functions in linear viscoelastic constitutive equations and related fractional operators. Math Model Nat Phenom 14:. https://doi.org/10.1051/mmnp/2018067
30. Miled B (2011) Coupled viscoelastic-viscoplastic modeling of homogeneous and reinforced thermoplastic polymers. PhD Thesis, Université Catholique de Louvain
31. Kaliske M, Rothert H (1997) Formulation and implementation of three-dimensional viscoelasticity at small and finite strains. Comput Mech 19:228–239. https://doi.org/10.1007/s004660050171
32. Hristov JY (2018) Linear viscoelastic responses: The prony decomposition naturally leads into the Caputo-Fabrizio Fractional Operator. Front Phys 6:. https://doi.org/10.3389/fphy.2018.00135
33. Jerabek M, Major Z, Lang RW (2010) Uniaxial compression testing of polymeric

materials. Polym Test 29:302–309.
https://doi.org/10.1016/j.polymertesting.2009.12.003
34. ASTM D575-91 (2014) Standard Test Methods for Rubber Properties in Compression. ASTM 91:2012–2015. https://doi.org/10.1520/D0945-16.2